Levofloxacin-loaded microneedles produced using 3D-printed molds for *Klebsiella pneumoniae* biofilm control

K. B. Vinayakumar[1,], Maria Daniela Silva[2], Artur Martins[1], Stephen Mundy[1], Pedro González-Losada[1], Sanna Sillankorva[1,*]*

K.B. Vinayakumar, S. Mundy, A. Martins, P. González-Losada, S. Sillankorva

INL - International Iberian Nanotechnology Laboratory, Av. Mestre José Veiga, 4715-330 Braga, Portugal

E-mail: vinaya.basavarajappa@inl.int, sanna.sillankorva@inl.int

M. D. Silva

Centre of Biological Engineering, University of Minho, Campus de Gualtar, 4710-057 Braga, Portugal

LABBELS—Associate Laboratory, Braga/Guimarães, Portugal

Keywords: microneedles, polyvinyl alcohol, levofloxacin, 3D printing, biofilms, *Klebsiella pneumoniae*

This article has been accepted for publication and undergone full peer review but has not been through the copyediting, typesetting, pagination and proofreading process, which may lead to differences between this version and the Version of Record. Please cite this article as doi: 10.1002/adtp.202200320.

Additive manufacturing advancements contribute considerably to several fields, and its use in the medical field is gaining attention due to its easily customizable option (patient-specific), low cost, and fast turnout time in developing drug delivery and diagnostic tools. Here, we report the fabrication of a microneedle (MN) platform using a stereolithography 3D printer, varying the 3D printing angle and aspect ratio (2:1, 3:1, 4:1). The optimal printing angle was 30º, resulting in needle tip and base diameters of ~50 µm and ~330 µm, and heights of ~550/850/1180 µm. Polyvinyl alcohol (PVA) MNs produced with varying levofloxacin concentrations showed variability of ~4% in tip and 3% base diameters and 15% in height compared to the 3D-printed MNs. Geometry B was used to produce levofloxacin-loaded PVA MNs and tested against *Klebsiella pneumoniae* colony biofilms. Levofloxacin was released gradually, as assessed by spectrofluorimetry. The MIC of levofloxacin against the *K. pneumoniae* clinical isolate was 4 µg/mL, but this concentration was insufficient to cause any effect on *K. pneumoniae* biofilms. Only concentrations ≥ 32 µg/mL were statistically different compared to the unloaded MNs. 3D printing is an attractive solution to produce molds for fabricating biopolymeric MNs for topical drug delivery.

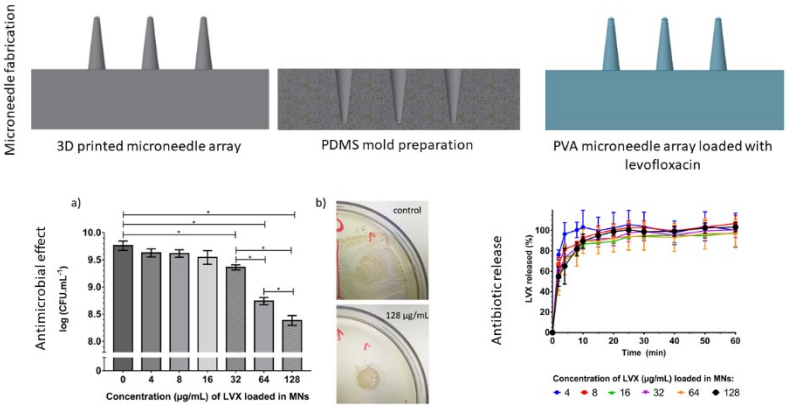

Improved transdermal delivery to Klebsiella pneumoniae biofilms was studied using levofloxacin-loaded polyvinyl alcohol microneedles. Microneedle arrays were printed in a stereolithography 3D printer, varying the needle length, geometry, and printing angle. The antibiotic-loaded microneedles significantly reduced the growth of K. pneumoniae compared to the unloaded microneedles, but the concentration required was > 8x MIC. The topical application of levofloxacin using microneedles can be a promising approach for treating biofilm-related topical infections.

1. Introduction

The skin has been a lucrative target for drug delivery and diagnosis in medicine. Since the skin is the largest organ in the body, various methods are being adapted to deliver drugs across the skin layers. A well-established method of drug delivery through the skin involves hypodermic needles. However, this conventional drug administration method does not deliver the drug effectively and accurately within the therapeutic range or window [1]. Hence, in the 1970s, a transdermal route was proposed to deliver the drug painlessly, more effectively, and accurately. Transdermal drug delivery technology has many advantages, such as targeting a specific skin area, avoiding the stomach environment, reducing medical costs and medical wastes, allowing a dose reduction, and more precise control over drug volume that can be achieved [2]. However, the main drawback of using a traditional transdermal patch is that the skin barrier is mostly impermeable, limiting the transport of large/hydrophilic molecules. Therefore, many alternative techniques have been proposed to improve transdermal drug delivery, such as jet injectors, iontophoresis, sonophoresis, chemical penetration enhancer, skin ablation, and microneedle [3,4]. Among these approaches, the microneedle approach is considered one of the best methods to deliver the drug with fewer side effects [3–6].

Since MNs are short, they do not reach the nerve-rich region resulting in less or no pain during insertion [4,7]. Also, MNs will help deliver macromolecules (e.g., insulin and vaccines), offering a patient-friendly drug administration. The primary use of microneedling is to create a pathway to an object by physically scratching or rupturing the top layer. In most applications, this barrier is the skin. The first concept of the microneedle array for the drug delivery application was reported by Gerstel and Place in 1971 [8]. This patent presents a concept of improved transdermal drug delivery using solid and hollow microneedle arrays [8]. Although the concept of microneedle was presented earlier, it was not fabricated until the 1990s, when the microfabrication revolution took place. Henry et al. reported the first 150 µm long microneedle array for the drug delivery application, showing a four orders magnitude increase in drug permeability through the skin compared to the traditional transdermal patches [9]. The strength of MNs as technological platforms has been demonstrated for different applications, such as electrical signal recording from the visual cortex of the brain [10], skin impedance measurement for cancer [11], insulin delivery [12], blood collection [13], among others (see [14] for a more detailed summary of the varied uses).

Different technologies such as deep reaction etching silicon (DRIE), laser machining metal, imprinting polymer, 3D printing polymer molds, and extruding polymer molding have been previously reported

to fabricate microneedle arrays [4,13,15–19]. Recent advancement in 3D-printing technology is increasingly accepted for developing MNs, microsensors, and microactuators [20–23]. Due to the skin thickness varying with ethnicity, gender, and age of people, the customizable MNs solution is crucial for applications related to drug delivery, antibody delivery, and interstitial fluid sampling, among others. The 3D printed molding approach will provide a customizable solution to produce a microneedle of interest in less time without the need for expensive equipment and trained microfabrication professionals [24,25]. The small cost, customizable approach, and easy-use nature of 3D printing were recently adopted to develop a microneedle array for drug delivery applications [26,27]. Kevin J. Krieger et al. reported using a stereolithography 3D printer to fabricate high aspect ratio microneedle masters and reproducing them in female silicone molds to fabricate dissolvable polymer MNs [27]. The developed approach showed a promising route to develop a MN array with a tip of ~20-30 µm. However, detailed studies on printing angle, MNs with different aspect ratios, and geometry variations concerning 3D-printed MNs and biopolymer needles have not been studied in detail. Further, the flexibility of the 3D printer for the specific application will allow the increase of the number of MNs per chip and modify the size, shape, and geometry of each microneedle just by modifying the design in the software.

MNs can be made of solid (e.g., metal, silicon, glass, and ceramics) or polymeric materials. The type of polymer used for the fabrication of MNs will have an impact on the characteristics of the MNs produced. For instance, the polymers chosen can create dissolving or hydrogel-forming MNs. Dissolving MNs are suitable for the delivery of low molecular weight drugs, enzymes, vaccines, peptides (reviewed in [28]), and even bacteriophages [29]. These are entirely or almost wholly dissolved once inserted into the skin. The materials used for this are water-soluble ones, including, for instance, maltose, dextran, and hyaluronic acid [30]. Hydrogel-forming MNs are swellable and are suitable, for instance, for the extraction of interstitial fluid and can be fabricated with diverse polymers, such as PMVE/MA, MeHA, silk, among others (reviewed in [31]). In recent years, polymeric MNs have received more attention in the biomedical area than inorganic and metal MNs, due to cost, biodegradability, biocompatibility, low toxicity, and strength [32,33].

This paper demonstrates the stereolithography-based 3D-printed approach to producing a microneedle array for drug (levofloxacin) delivery for medical applications. The design and fabrication of the different printing angles have been evaluated to find the optimum printing conditions. An optimized printing angle was chosen and used to produce arrays of the 3D-printed MNs with different aspect ratios. Printed MNs were subsequently used to produce PDMS molds and

biopolymer microneedle arrays loaded with levofloxacin. In addition, MNs with different base geometries were produced to find the robustness of the 3D printing system. *Klebsiella pneumoniae* is one of the most common pathogens in nosocomial infections. In recent years, this bacteria has been associated with chronic ulcers and burn wound infections, besides severe pulmonary and urinary tract infections [34,35]. The presence of this pathogen in wounds is problematic since it is often associated with biofilms that are increasingly resistant to antibiotic treatment [36]. Nonetheless, the delivery using MNs can prompt a drug distribution to layers, often not accessible due to the biofilm matrix surrounding the bacterial cells, and the mechanical effect can already cause some damage in the 3D biofilm structures. Therefore, MNs with different levofloxacin concentrations were assessed for their effectiveness in reducing the number of viable *K. pneumoniae* cells in biofilms.

2. Results and Discussion

2.1. Microneedle design and 3D printing

The MNs designed in the manuscript have a tip diameter of 50 µm, base diameter of 300 µm, and height of 600/900/1200 µm. A study by Gill et al. demonstrated that a microneedle with a tip radius of 50 µm could enable easy and pain-free insertion into the skin [37], and the microneedle height will depend on the region at which the drug molecule that needs to be delivered under the skin. The typical needle height required to rupture the top layer of the skin is ~150 µm [9]. However, different aspect ratios (2:1, 3:1, 4:1) of MNs were demonstrated to address the 3D-printed microneedle scope in delivering the drug in different skin layers for potential application in drawing interstitial fluids [24–27].

The Z resolution influence on stepping, i.e., the smoothness of the microneedle, was studied by Ashley R. Johnson et al. [26]. A higher printing resolution takes a long time to print but should create a smoother surface on features. The smoothness of the needle is crucial to reduce the insertion force and ensure the easy extraction of the cured part from the master mold. Another parameter optimized is the distance between adjacent needles. When the distance between the needles is too small, the resin between them can occasionally and randomly be fused. This consequently affects

the microneedle outer wall angle out in a concave shape. The orientation of the printing angle showed a considerable influence on the microneedle geometry.

Along with the variation in needle geometry, needles were tilted or twisted with printing angle orientation. **Figure 1** shows optical and SEM images of the MNs printed considering the parameters detailed in the experimental section.

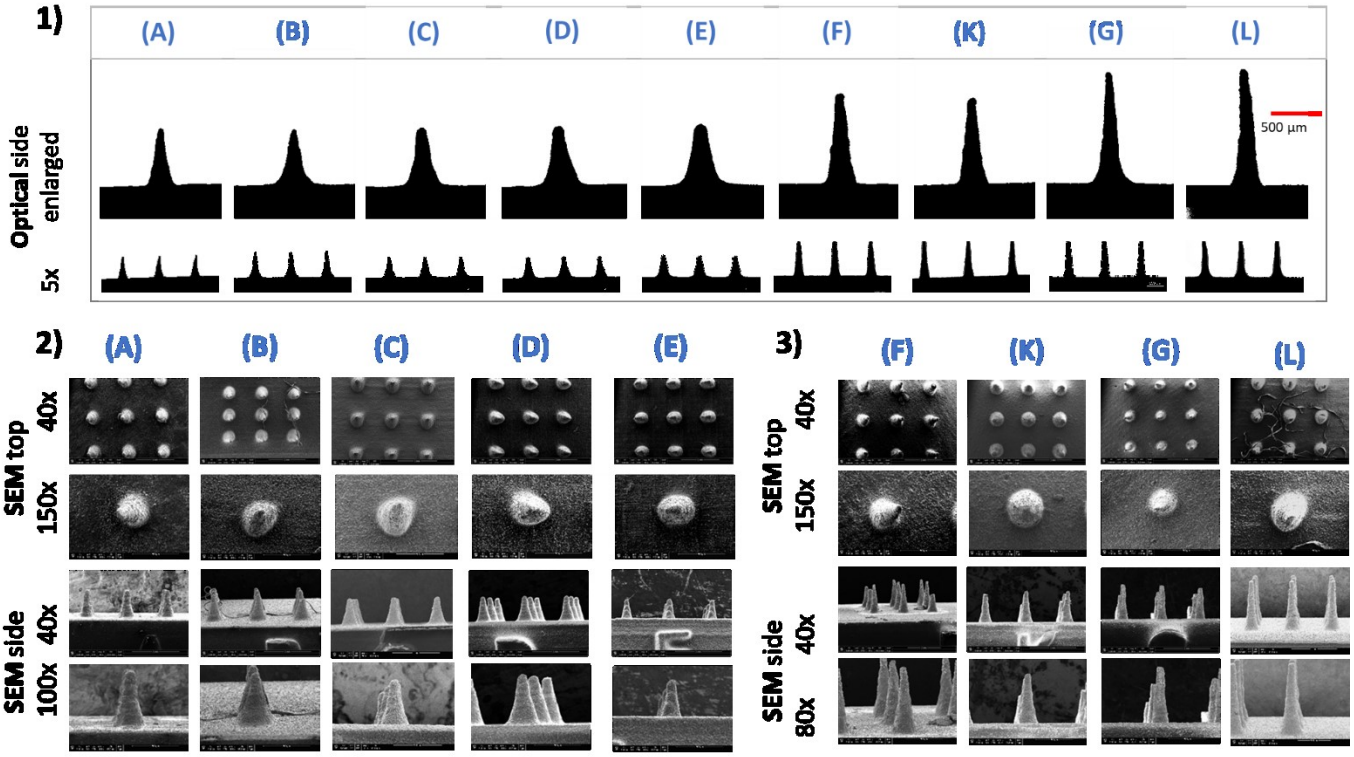

Figure 1. Optical and SEM microscopy of different MNs. 1) Optical microscopy of the different MNs. The upper figures are enlarged MNs from the strip with three MNs printed on the strip edge taken using a 5× objective. 2) SEM microscopy of arrays with a height of 600 µm and printed at different angles, 3) MNs with heights of 900 and 1200 µm printed at 0° and 30° angles.

The variation in tip, base, and height of printed MNs with different printing angle orientations and the designed CAD model geometries for each parameter were analyzed (**Figure 2**).

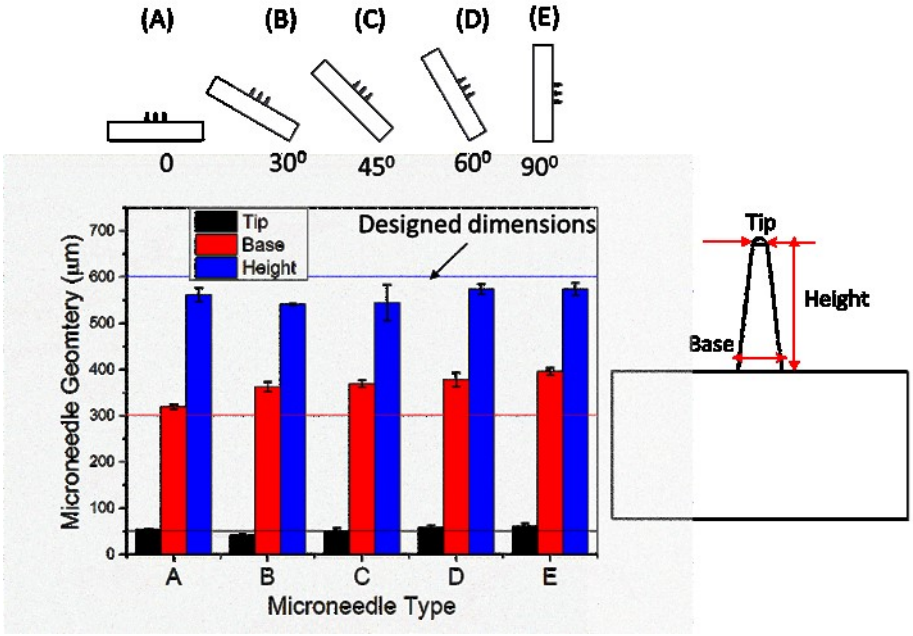

Figure 2. Microneedle angle orientations used during printing, and the different geometries designed using CAD (tip-horizontal black, base-red, and height-blue lines) and the 3D printed MNs (columns using the same colors).

MNs printed with 0^{o} showed a more repeatable result concerning the needle tip, base, and height with the designed CAD model geometries. However, the drawback observed in the 0^{o} printing is tilting the MNs towards one direction. The tilting of a tip can be due to the pulling force generated during the resin pulling all along the printing process. Printing with 30^{o} orientation showed a promising result with the reduction in tilting of the needles. However, the obtained needle geometry is not closely related to the 0^{o} printed needles. The reduction in the tip radius is interesting for the microneedle application. The reduction in microneedle tip radius can be due to the printing angle, which needs to be studied in detail. However, the observed reduction in tip diameter is relatively consistent. Other printed orientations (45^{o}, 60^{o}, 90^{o}) showed promising repeatable results, but the needle tip diameter is greater than the 30^{o} orientation printed needles.

After understating the variability of each parameter during different printing orientations, 30^{o} was used to print 11×11 MNs arrays. The 3D-printed microneedle arrays fabricated were used to produce PDMS molds, which were used to produce biopolymer MNs.

The 3D printed microneedle arrays using the 30^{o} orientation were observed by scanning electron microscope (SEM) (**Figure 3** (1-3)).

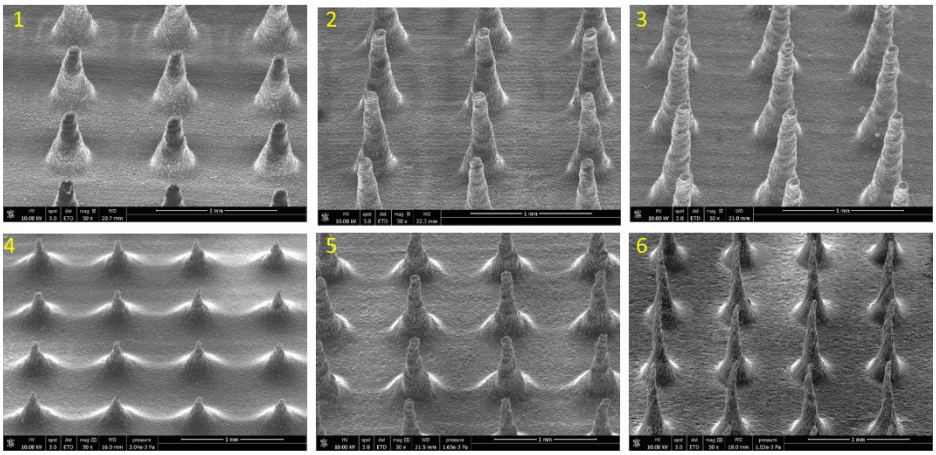

Figure 3. Microneedle arrays. 1) 3D printed microneedle mold with 2:1 aspect ratio, 2) 3D printed microneedle mold with 3:1 aspect ratio, 3) 3D printed microneedle mold with 4:1 aspect ratio, 4) PVA microneedle using mold-1, 5) PVA microneedle using mold-2, 6) PVA microneedle using mold-3.

The SEM images show that >95% of the 3D printed MNs were intact (few broken needle tips were observed in the high aspect ratio MNs). We believe the broken needles were primarily related to the handling of the sample. It has been validated that an optimized SLA recipe can generate a robust microneedle array with a large variety of geometries.

The traditional approach to producing biopolymer-based MNs still depends on cleanroom-processed silicon molds. One of the main drawbacks of silicon-processed mold is that it is difficult to achieve 3D features on the molds. However, the capability of achieving complex features/geometries, fast turnaround time, and low-cost production have helped the adoption of 3D printing in different application sectors, such as surgical tools, medical applications, organ-on-chip, tissue engineering, and patient-specific implants [38]. On the scalable fabrication side, SLA 3D printers can help to produce robust and custom molds using the wide variety of material libraries available from the supplier (https://formlabs.com/materials/engineering/). These materials withstand high temperatures and pressure making them suitable for injection molding of the polymer microneedle array [39,40]. **Table 1** summarizes the literature on 3D-printed microneedle molds used for drug delivery applications.

Table 1. 3D printed microneedle molds produced using different methods and their geometries

Ref.	Method	Height (µm)	Base (µm)	Tip (µm)
[41]	Continued liquid interphase production (CLIP)	1000	333	
[42]	Direct laser printing (DLP)	700	250	
[27]	SLA	3000/1000/600		40-80
[26]	SLA (with 25 µm layer thickness)	707	437	40
This work	SLA	1180/850/550	330	40-50

Along with obtaining similar results concerning needle geometry, the effect of printing angle on the needle tip tilting is studied in the manuscript. Furthermore, MNs with different base geometry (square, circle, triangle, pentagon, and hexagon) have also been successfully printed with good repeatability (**Figure 4**).

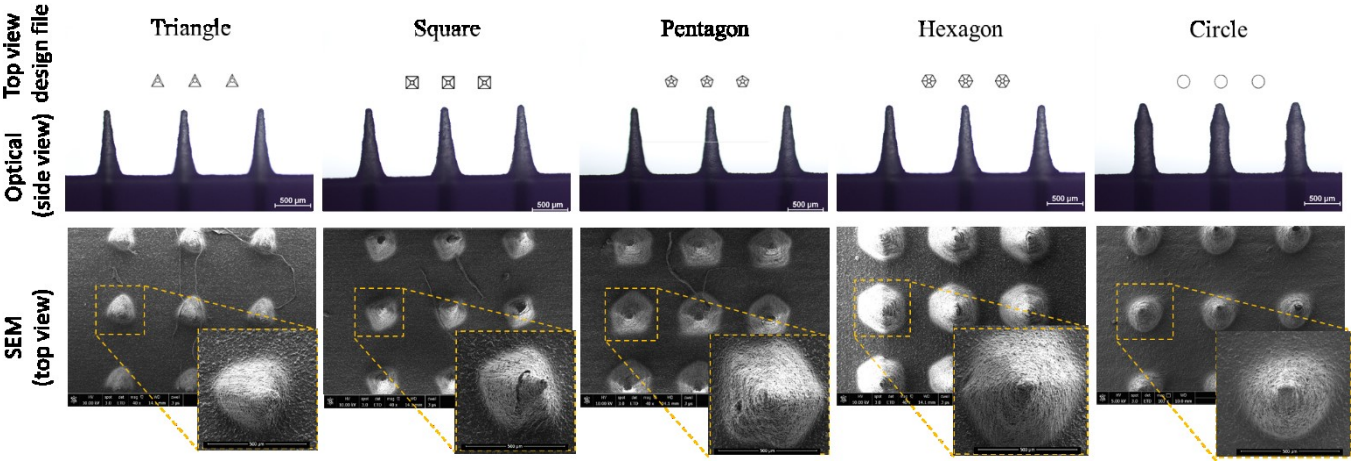

Figure 4. 3D-printed microneedle molds with different base geometries. Top - optical microscope images (5× objective). Bottom - SEM micrographs of the array and an enlarged microneedle.

Achieving silicon micromachining with such diverse geometries is always challenging and complicated. Hence, this result validates the robustness and ease of use nature of the 3D printer in micro-molding applications compared to traditional silicon processing.

2.2 Biopolymer microneedle fabrication

Three different aspect ratio MNs were 3D-printed and used to produce PDMS molds. The produced PDMS molds were used to fabricate biopolymer MNs. PVA MNs, fabricated using different aspect ratios, were observed by SEM (**Figure 3** (4-6)). PVA is a synthetic polymer approved by the FDA and commonly used in medical devices because of its biocompatibility, non-toxicity, and non-carcinogenicity due to its inertness and stability. For instance, Bushan et al. tested the cytotoxicity of different wearable wound sensor constituents and found that their polyvinyl alcohol-based polymer (PVA-SbQ) had excellent biocompatible with keratinocytes (cell viability >90%), being minimally toxic to these cells [43]. In another study, fibroblasts and keratinocytes exposed for 24 h to highly porous membranes of N, O-carboxymethyl chitosan (CMCh) and PV) resulted in a 80-100% cell viability for both cell lines, showing no significant cytotoxic effect [44]. In addition, PVA has low protein adsorption and high water solubility and chemical resistance characteristics. Moreover, PVA is an excipient available in pharmaceutical-quality raw material in quantities required for large-scale commercial use and is widely used in wound dressings due to its moisturizing effect and ability to absorb wound exudate [45,46].

Figure 5 summarizes the geometrical variation between 3D-printed MNs with biopolymer MNs, using the MNs with a height of 900 µm.

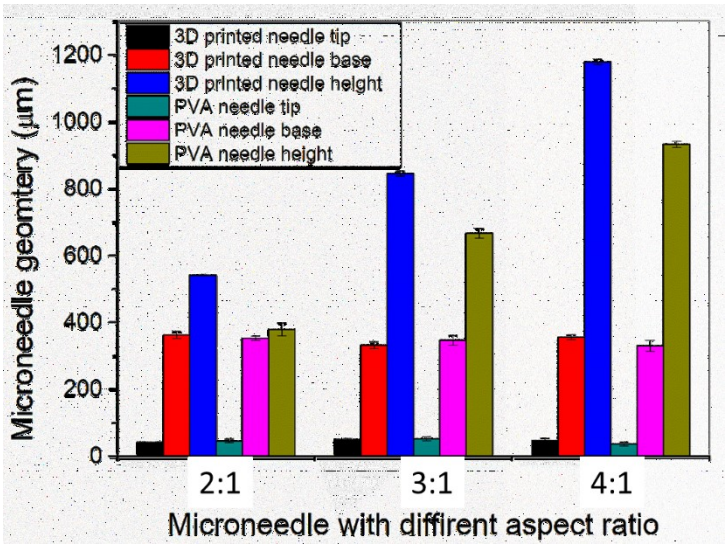

Figure 5. Printed and biopolymer microneedle geometries for different aspect ratio MNs.

The tip and base diameter of the biopolymer MNs are consistent with the 3D-printed microneedle, with a variability of less than ~2%. However, the height of the microneedle showed a considerable variation between 3D-printed and biopolymer MNs. The significant variation is seen in the microneedle with a 2:1 aspect ratio, where the reduction in biopolymer microneedle height is ~32% compared to the 3D printed microneedle. In the 3:1 and 4:1 MN aspect ratios, a reduction of ~11% in the biopolymer needle height was seen compared to the 3D-printed MNs. This difference in height phenomena of the polymer MNs versus the master mold was observed already with other polymers (alginate, carboxymethyl cellulose, and hyaluronic acid), which varies with the concentration of polymer used [47]. For instance, the master mold was 1200 µm in height, and the MNs produced using the PDMS replica varied in height from 971 µm [carboxymethyl cellulose 5% (w/w)] up to 1077 µm [hyaluronic acid 1% (w/w)], corresponding to reductions ~19% to ~10%. Furthermore, increasing the polymer concentration also caused an increase in the height of hyaluronic acid MNs [1012 µm with 1% (w/w) to 1077 µm with 5%] but decreased the height of carboxymethyl cellulose MNs [1086 µm with 1% (w/w) to 971 µm with 5%]. The difference in microneedle height can be controlled by optimizing the PDMS hardness, PDMS curing temperature, controlling the vacuum processing during PVA needle development, and using a more suitable polymer selection and its concentration.

2.3. Production and efficacy of the levofloxacin (LVX) loaded MNs

Envisioning using these MNs in biofilm-related infections, *K. pneumoniae* was selected as the bacterial pathogen for the studies as this gram-negative species is frequently isolated from infected wounds, including chronic wounds. In addition, the antibiotic levofloxacin (LVX) was chosen since it can be used for treatment and can be detected by fluorescence spectroscopy, which is advantageous for its rapid quantification.

2.3.1.Minimum Inhibitory Concentration (MIC)

The MIC of LVX against *K. pneumoniae* PC28 planktonic cells was 4 µg/mL (**Figure 6**). According to the EUCAST clinical breakpoints, *K. pneumoniae* is resistant to LVX at dosings higher than 1 µg/mL.

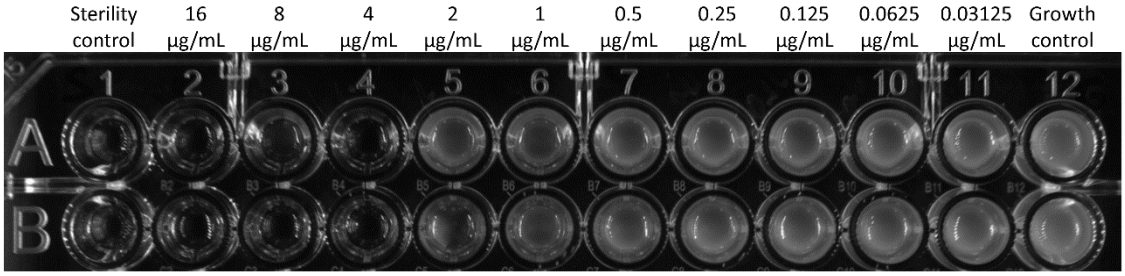

Figure 6. Determination of the minimum inhibitory concentration of levofloxacin *on K. pneumoniae* PC28. Image acquired using Chemi XT4.

2.3.2.Antibiofilm activity of levofloxacin-loaded MNs against K. pneumoniae biofilms

K. pneumoniae biofilms were formed for 24 h, treated with LVX-loaded MNs for an additional 24 h, and quantified (**Figure 7a**). Although different geometries were printed in this work, for the release and antimicrobial efficacy studies, only one of these geometries was tested (B geometry, see Table 2). Furthermore, although in planktonic cells, the MIC concentration obtained was 4 µg/mL, it is well known that antibiotic concentrations needed to cause a reduction of biofilm cells are generally higher. Within biofilms, their self-produced extracellular polymeric matrix protects cells from antibiotic action. Moreover, the lower cell growth rate and the presence of metabolically inactive cells also contribute to the increased antibiotic tolerance of biofilms compared to planktonic cells [48].

Therefore, in this study, a minimum concentration equal to the MIC (4 µg/mL) and a maximum concentration of 128 µg/mL (32× MIC) was loaded onto the MNs.

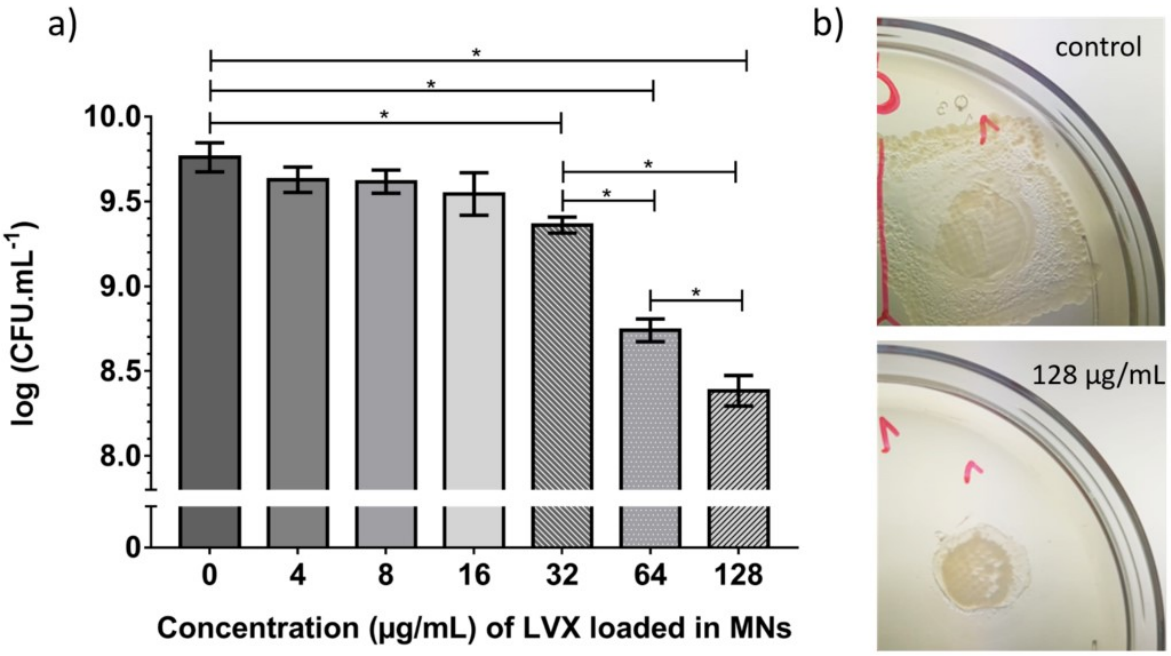

Figure 7. Levofloxacin-loaded MNs. a) antibiofilm effect measured as the logarithmic number of *K. pneumoniae* PC28 viable cells from 24-h biofilms after 24 h of treatment with levofloxacin-loaded MNs. Data are shown as mean ± SD for n = 3. Differences were considered statistically significant if P ≤ 0.05 (*). b) efficacy of the levofloxacin-loaded MNs on colony biofilms.

Levofloxacin is only available in oral and intravenous formulations, and its administration involves daily dosages of 250 to 750 mg [49,50]. The disadvantages of systemic administration of antibiotics are well-known, including several side-effects (particularly in the gastrointestinal tract), impact on commensal flora, low bioavailability at the infected region, and increase of antimicrobial resistance [51]. The topical application of antibiotics, for instance, using MNs, minimizes these effects. Moreover, MNs are an attractive choice for biofilm infections since they can penetrate the extracellular polymeric matrix barrier and deliver the loaded antimicrobial into the biofilm interior [29,52,53].

The viable cells reached a concentration of 9.76 $\log_{10}$CFU/mL (Figure 7a). As expected, LVX-loaded MNs significantly reduced *K. pneumoniae* biofilm cells only at LVX concentrations ≥ 32 µg/mL (P≤0.05) compared to the unloaded MNs. Therefore, a concentration 8 times higher than the MIC was

necessary to produce a noticeable effect on biofilms. From this concentration forward, all viable cell counts were statistically different (P≤0.05), not only from the control (unloaded MNs) but also between each concentration. Nevertheless, biofilm eradication was not achieved.

The delivery of LVX using MNs was previously studied to control biofilms formed by other bacterial species. Polydopamine nanoparticles containing levofloxacin and α-amylase were incorporated into MNs and used to treat *Staphylococcus aureus* and *Pseudomonas aeruginosa* biofilms. A residual biofilm biomass of only 12.63 ± 1.86% was obtained after treatment (versus 100% of the untreated control). The antibiofilm effect was also evaluated *in vivo* in a rat model of infected full-thickness skin defect. The MNs incorporating polydopamine nanoparticles loaded with levofloxacin with and without α-amylase reduced the bacterial levels. Photothermal therapy further reduced the number of bacteria, with almost eradication ability [53].

There are also major visual differences between the unloaded and LVX-loaded MNs on colony biofilms formed on the Petri dishes (Figure 7b). As visible, the biofilms where unloaded MNs were used (control) spread throughout the agar layers, occupying a large area, while in the LVX-treated colony biofilms, the biomass is restricted to the area where the polycarbonate membrane was placed. Only the viable cells in the polycarbonate membrane were counted for the viable cell counts since the area covered by the biomass on the Petri dishes using different antibiotic concentrations was highly dependent on the LVX concentration used.

The mechanical behaviour of the the PVA MN arrays varying in length and geometry was investigated (Figure 8).

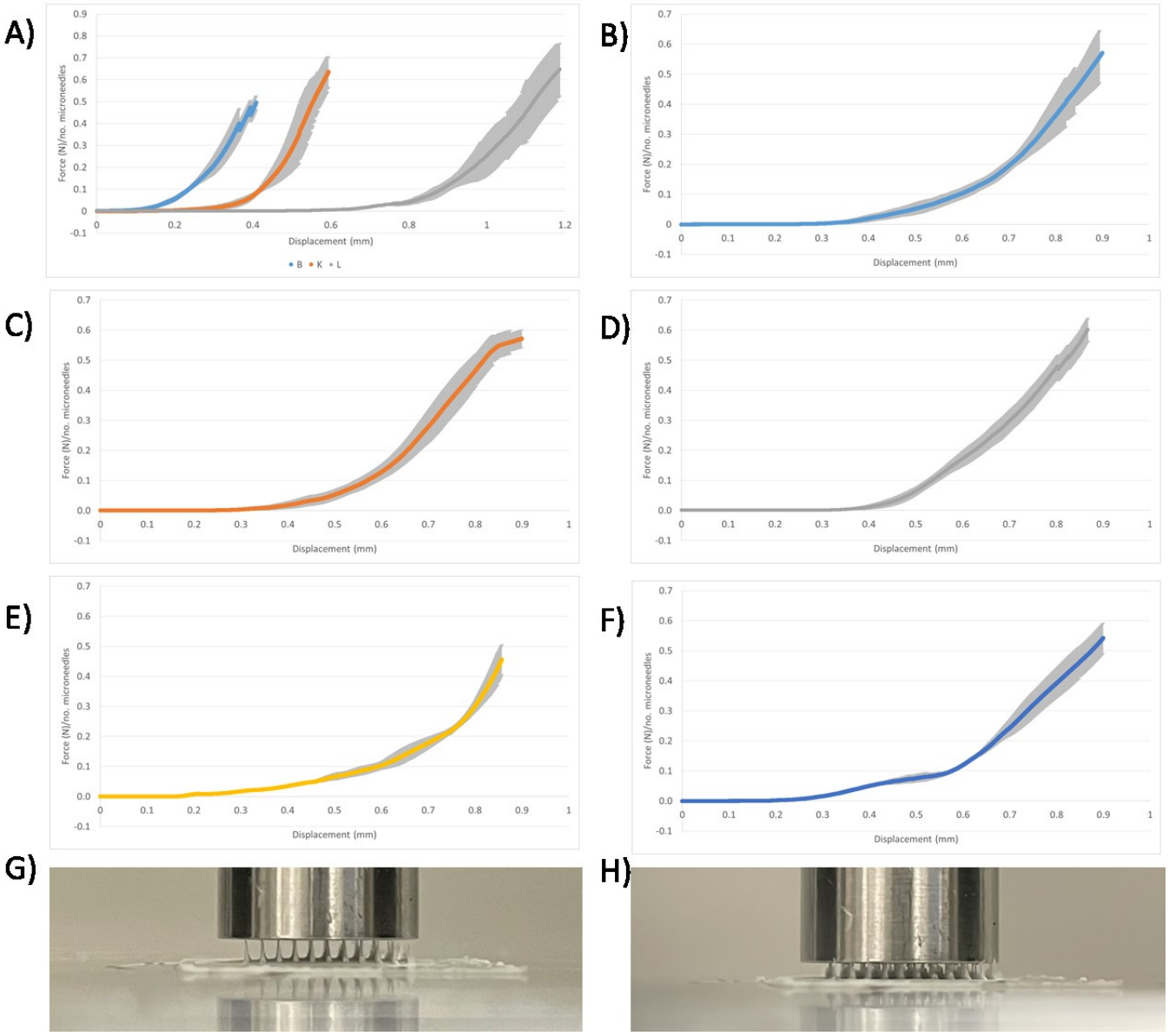

Figure 8. MN force-displacement curves (A-F) and images of MNs subjected to the test (G-H). A) Arrays B, K, and L; B) triangular geometry; C) square geometry; D) pentagon geometry; E) hexagon geometry, and F) circle geometry.

There were no significant differences between the PVA MN arrays varying in height and geometry. Furthermore, the curves did not show a transition point which could indicate buckling failure. This is in agreement with other studies reported in the literature [54–56]. The only exception is the geometry depicted in Figure 8F, which showed a curve with a changing slope before fracture force was reached, most likely due to bending. There were, however, slight differences in the mechanical behaviour over

the displacement ranges of PVA arrays varying the geometry (Fig 8B-8F). Since all were fabricated with PVA, the change is attributed merely to the geometry of the MNs.

2.3.3.Release of levofloxacin from the PVA MNs

The release of LVX from the microneedle arrays at different concentrations was assessed for 60 min (**Figure 9**).

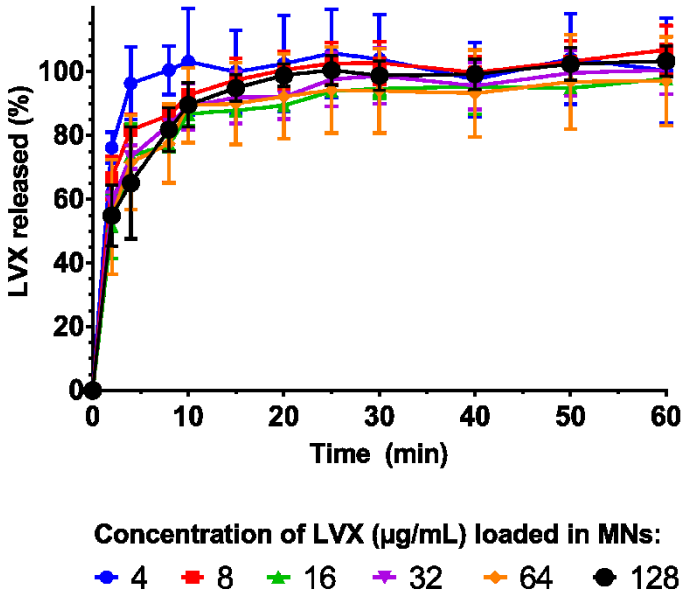

Figure 9. Percentage of levofloxacin released from the MNs loaded with different levofloxacin concentrations (4 to 128 µg/mL). Data are shown as mean ± SD for n = 3. Differences were considered statistically significant if $P \leq 0.05$ (*).

The release started immediately, and after approximately 10 min, the curves reached a plateau, with approximately the total concentration (100%) loaded being released. This is because the polyvinyl alcohol used is known to dissolve quickly (7-11 min) [29].

The MNs can, therefore, deliver a high amount of antibiotic quickly, resulting in higher bioavailability and faster onset of action than, for instance, topical creams and transdermal patches. It is reported that only 10 to 20% of drugs applied using topical creams can permeate across the skin. In the case of transdermal patches, the drug also still has to permeate the stratum corneum. Using hypodermic

needles, the drug is delivered directly into the dermis, providing high bioavailability and fast action like MNs, but it is very painful, and self-administration is not possible [57]. Also, as stated before, MNs can penetrate the extracellular polymeric matrix of biofilms, which does not happen with topical creams and transdermal patches.

3. Conclusion

The manuscript reports desktop SLA printer optimization to print high aspect ratio microneedle arrays for biomedical applications. In addition, the effect of microneedle geometry due to printing angle orientation is reported. Fabricated different aspect ratios (2:1, 3:1, 4:1) MNs were used to produce PDMS molds and subsequent biopolymer (PVA) microneedle arrays using the PDMS molds. The fabricated biopolymer MNs with different aspect ratios were compared with the 3D-printed MNs, and although they were closely related, the variation in microneedle height needs to be studied by optimizing the PDMS molding process and biopolymer microneedle fabrication process. The dissolving polymeric MNs had an effect in locally reducing the concentration of viable cells of *K. pneumoniae* from biofilms. Antimicrobial-loaded MNs can have benefits when dealing with hard-to-remove biofilms from, for instance, chronic and infected wounds and should be explored more as possible alternatives to systemic drug delivery.

4. Experimental Section/Methods

The 3D microneedle printing process: Microneedle master molds, varying in geometry, were fabricated using a Formlabs Form2 desktop 3D stereolithography (SLA) printer. A standard grey resin (RS-F2-GPGR-04, Formlabs) was used, and during the SLA 3D printing, the liquid resin was cured by a highly accurate laser to form each layer achieving much finer details and repeatedly achieving high-quality results. This is particularly important for printing fine intricate geometry with smooth surfaces such as MNs. Although SLA printers can usually achieve significantly smaller layer thickness (Z-axis), the reason for improved print quality compared to FDM printers lies in their much higher XY resolution. To ensure optimal printing conditions, the Form2 SLA printer was inspected and checked for potential issues that might affect the print quality before printing. The optical glass window was cleaned using a dry lint-free wipe (PEC Pad), and the resin was filtered using a 190-micron mesh oil.

The grey resin MN fabrication workflow consisted of 3 steps: Design, Printing, and Post-processing. First, a 3D CAD model of the MN array (MNA) was created using Autodesk Inventor 2014 CAD software. Next, a .stl file was exported from Inventor and imported into the proprietary SLA software, Preform. Preform enabled the user to define the printing parameters. After printing, the MNA was washed in clean isopropyl alcohol (IPA) bath for 10 min. The bath used a magnetically coupled impeller to agitate the IPA to remove the non-solidified resin effectively. Later, the MNA was dried at room temperature (RT) for 30 min and cured by UV (405 nm) for 60 min at 60 ºC. Printing angles of 0, 30, 45, 60, and 90º (**Figure 10**) were tested to study the microneedle variations in height, length, and base diameter compared to the designed CAD model.

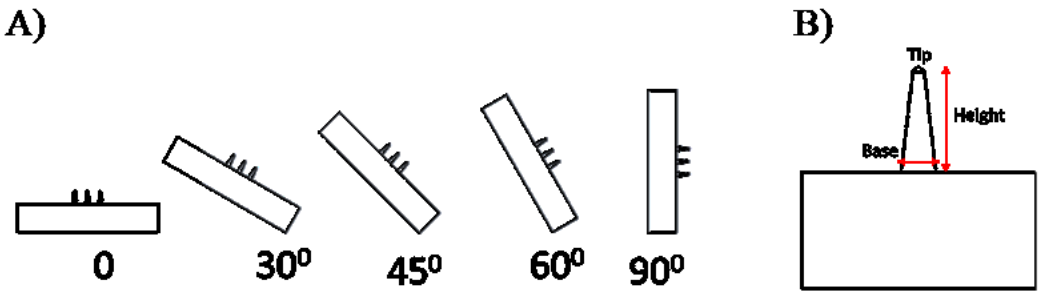

Figure 10. (A) Printing angles used in microneedle fabrication steps and (B) a schematic representation of where the height, tip, and base dimensions were determined.

The CAD model of the microneedle in the study was designed with a tip radius of 50 µm, base diameter of 300 µm, and height of 600 µm, 900 µm or 1200 µm to obtain an aspect ratio of 2:1, 3:1, and 4:1 (**Table 2**).

Table 2. Geometries of the 3D-printed MNs

Label	Diameter (µm)	Height (µm)	Ratio	Radius	Pitch*	Printing orientation (º)
A						0
B	300	600	2:1	50	90	30
C						45

D			60
E			90
F	900	3:1	0
K			30
G	1200	4:1	0
L			30

*Pitch – the distance between the needles.

After optimizing the printing angle, using just three printed MNs printed at the edge, a master MNA was created, with which a female PDMS mold (see 2.2) and the biopolymeric MNA (see 2.3) were developed (**Figure 11**).

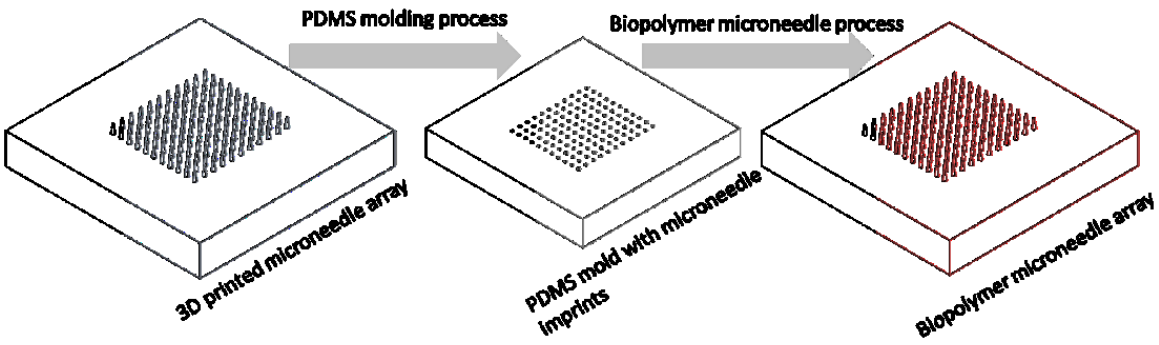

Figure 11. Biopolymer microneedle array fabrication steps.

PDMS mold fabrication: The 3D-printed MNA master mold was used to produce a polydimethylsiloxane (PDMS) replica. First, the mold was placed into a desiccator with a drop of trichloro (1,1,2,2-perfluorooctyl) silane (from Sigma-Aldrich) and placed under vacuum conditions, causing the silane to evaporate and form a layer on the surface of the mold to prevent any PDMS adhesion. The PDMS (Sylgard 184 from Dow Corning) was prepared by mixing elastomer and curing agent (10:1 ratio), followed by 3 min of sonication to mix both components homogeneously. Then, the PDMS was placed for 15 min in the desiccator under vacuum conditions to remove all air bubbles generated during the sonication. Next, the PDMS was poured onto the MNA master, and a vacuum

was applied for 30 min to remove any remaining bubbles. Finally, the PDMS mold was cured overnight in an oven at 70 ºC. The resulting PDMS replica was easily removed from the master mold without causing damage to the 3D-printed grey resin MNA.

Biopolymer microneedle fabrication process: Polyvinyl alcohol (PVA, Mowiol 4:88, Sigma Aldrich, MO, USA) was used to fabricate MNs with and without levofloxacin (LVX) using a molding technique. PVA [10% (w/v)] was hydrated in sterile water for four h at RT under agitation (350 rpm). After, the temperature was increased to 85°C and, under agitation (350 rpm), PVA was allowed to dissolve completely for approximately three h. The solution was allowed to cool, and after, LVX in water was mixed with the solution to have final concentrations ranging from 4 to 128 µg/mL. A volume of 150 µL of PVA was placed in the PDMS molds, and a vacuum was applied (Agilent Technologies IDP3, Massachusetts, USA). Molds were centrifuged at 1000 rpm (RT, 10 min, Universal 320, Hettich GmbH & Co. KG., Tuttlingen, Germany) to fill the microneedle cavities and remove air bubbles completely. The polyvinyl MNs were dried for three h at 40°C in a ventilated oven (Termaks B8054, Bergen, Norway). MNs in their respective PDMS molds were stored in vacuum-sealed bags at 4 ˚C until their manual removal from the PDMS molds for further use. To perform anti-biofilm experiments, MNA were fabricated using filter sterilized PVA solution containing different LVF concentrations that were poured to UV sterilized (15 min UV) PDMS moulds. Vacuum filling and drying were performed in closed Petri dishes.

Compression experiments

Compression experiments were performed using a Shimadzu AGX-10kN Texture Analyzer (Shimadzu, Japan) equipped with a 500 N load cell and a 10 mm (diameter) cylindrical probe. At least 3 replicates of each sample were tested. The tested conditions involved a compression speed of 0.01 mm.s-1 (equivalent probe pulling speed) with a complete travel of up to 1.2 mm maximum.

Bacteria and growth conditions: The *K. pneumoniae* PC28 (clinical isolate, Hospital de Braga) used in this study was previously described to be a *K. pneumoniae* carbapenemase (KPC) [58]. The strain was grown at 37 ˚C in Tryptic Soy Broth (TSB) or Tryptic Soy Agar (TSA).

Minimum inhibitory concentration (MIC): The minimum inhibitory concentration (MIC) of LVX (Alfa Aesar, MA, USA) for *K. pneumonia*e PC28 was determined using the broth microdilution method according to the guidelines of the Clinical and Laboratory Standards Institute. The 96-well plate was imaged using a high-performance imaging apparatus (Chemi XT4, GBOX-CHEMI-XT4-E, AlphaMetrix Biotech, Rödermark, Germany), coupled with a 4.2 MP imaging 16-bit CCD camera.

Antibiofilm activity of LVX-loaded PVA MNs: The activity of LVX-loaded MNs was evaluated against 24 h-biofilms of *K. pneumoniae* PC28. Biofilms were produced according to the colony biofilm procedure [29], with some modifications. Briefly, overnight cultures of *K. pneumoniae* were diluted to an approximate concentration of 1×10^8 CFU/mL. Sterile polycarbonate membranes (Whatman® Nuclepore™ Track-etched, Maidstone, UK, 25 mm diameter, 0.1 µm pore size) were cut to the size of the MNA and placed on TSA plates with the shiny side facing up and inoculated with 50 µL of this culture. The polycarbonate membranes were incubated at 37 ˚C under static conditions for 24 h and transferred to fresh TSA plates. Next, unloaded and LVX-loaded MNs were placed on top of the 24 h-biofilms formed on the polycarbonate membranes. After, the plates were incubated at 37 ˚C. After 24 h, the polycarbonate membranes were removed and placed on 1 mL of saline (0.9% (w/v) NaCl). The samples were vortexed thoroughly, serially diluted in saline, and plated on TSA to quantify the number of CFUs.

Levofloxacin release from the MNs: The release of LVX from the MNs at 37 ˚C was evaluated. Briefly, MNs loaded with different concentrations of LVX (4 to 128 µg/mL) were removed from the PDMS molds, placed in 5 mL of water, and incubated at 37 ˚C under agitation (120 rpm) (Advanced 3500 Orbital Shaker, VWR). Samples (200 µL) were taken every 2 min until 10 min, every 5 min until 30 min, and every 10 min until 60 min. The LVX concentration was determined by spectrofluorimetry (excitation at 295 nm and emission at 440 nm) using a microplate reader (SYNERGY H1 Biotek). The data was presented as the cumulative percentage of LVX released.

Optical and scanning electron microscopy visualization: Lateral views of the 3D-printed MNA master molds and PVA MNs were acquired with a wide-field upright optical microscope (Nikon – Eclipse Ni-E, Japan) coupled with a one-color camera (DS-Fi2, Nikon, Japan). The microneedle arrays (3D printed and PVA) were sputtered with gold (Leica Microsystems, EM ACE200, Wetzlar, Germany) and visualized by scanning electron microscopy (Quanta FEG 650, FEI Europe B.V., Eindhoven, Netherlands).

Statistical analysis: Mean and standard deviations (SD) were determined for at least three independent experiments (n). Statistical comparison was performed using One-Way ANOVA and Tukey's multiple comparisons test through GraphPad Prism 7 software. Differences were considered statistically different if $P \leq 0.05$ (95% confidence interval).

Acknowledgements

Sanna Sillankorva acknowledges funding by FCT through the individual scientific employment program contract (2020.03171.CEECIND).

Received: ((will be filled in by the editorial staff))
Revised: ((will be filled in by the editorial staff))
Published online: ((will be filled in by the editorial staff))

References

[1] S. Adepu, S. Ramakrishna, Controlled drug delivery systems: Current status and future directions, Molecules. (2021). https://doi.org/10.3390/molecules26195905.

[2] N. Dragicevic, H.I. Maibach, Percutaneous penetration enhancers chemical methods in penetration enhancement: Nanocarriers, 2016. https://doi.org/10.1007/978-3-662-47862-2.

[3] D. Ramadon, M.T.C. McCrudden, A.J. Courtenay, R.F. Donnelly, Enhancement strategies for transdermal drug delivery systems: current trends and applications, Drug Deliv. Transl. Res. (2022). https://doi.org/10.1007/s13346-021-00909-6.

[4] W.Y. Jeong, M. Kwon, H.E. Choi, K.S. Kim, Recent advances in transdermal drug delivery systems: a review, Biomater. Res. (2021). https://doi.org/10.1186/s40824-021-00226-6.

[5] J. Hadgraft, M.E. Lane, Skin: The ultimate interface, Phys. Chem. Chem. Phys. (2011). https://doi.org/10.1039/c0cp02943b.

[6] Y.C. Kim, J.H. Park, M.R. Prausnitz, Microneedles for drug and vaccine delivery, Adv. Drug Deliv. Rev. (2012). https://doi.org/10.1016/j.addr.2012.04.005.

[7] I.H. Bajwa, N. Kaur, J.M. Dsouza, J.L. Mathew, Evaluation of efficacy and safety of intradermal delivery of vaccines through microneedle(s) in human beings: a protocol for a systematic review, Syst. Rev. 11 (2022) 170. https://doi.org/https://doi.org/10.1186/s13643-022-02046-8.

[8] M.S. Gerstel, V.A. Place, Drug Delivery Device, US-3964482-A, 1976.

[9] S. Henry, D. V. McAllister, M.G. Allen, M.R. Prausnitz, Microfabricated microneedles: A novel approach to transdermal drug delivery, J. Pharm. Sci. (1998). https://doi.org/10.1021/js980042+.

[10] P.K. Campbell, K.E. Jones, R.J. Huber, K.W. Horch, R.A. Normann, A Silicon-Based, Three-Dimensional Neural Interface: Manufacturing Processes for an Intracortical Electrode Array, IEEE Trans. Biomed. Eng. (1991). https://doi.org/10.1109/10.83588.

[11] P. Åberg, P. Geladi, I. Nicander, J. Hansson, U. Holmgren, S. Ollmar, Non-invasive and microinvasive electrical impedance spectra of skin cancer - A comparison between two techniques, Ski. Res. Technol. (2005). https://doi.org/10.1111/j.0909-725X.2005.00125.x.

[12] K.B. Vinayakumar, P.G. Kulkarni, M.M. Nayak, N.S. Dinesh, G.M. Hegde, S.G. Ramachandra, K. Rajanna, A hollow stainless steel microneedle array to deliver insulin to a diabetic rat, J. Micromechanics Microengineering. (2016). https://doi.org/10.1088/0960-1317/26/6/065013.

[13] K. Oka, S. Aoyagi, Y. Arai, Y. Isono, G. Hashiguchi, H. Fujita, Fabrication of a micro needle for a trace blood test, in: Sensors Actuators, A Phys., 2002. https://doi.org/10.1016/S0924-4247(01)00872-X.

[14] P. Dardano, M. Battisti, I. Rea, L. Serpico, M. Terracciano, A. Cammarano, L. Nicolais, L. De Stefano, Polymeric Microneedle Arrays: Versatile Tools for an Innovative Approach to Drug Administration, Adv. Ther. (2019). https://doi.org/10.1002/adtp.201900036.

[15] L.R. Pires, K.B. Vinayakumar, M. Turos, V. Miguel, J. Gaspar, A perspective on microneedle-based drug delivery and diagnostics in paediatrics, J. Pers. Med. (2019). https://doi.org/10.3390/jpm9040049.

[16] M. Azmana, S. Mahmood, A.R. Hilles, U.K. Mandal, K.A. Saeed Al-Japairai, S. Raman, Transdermal drug delivery system through polymeric microneedle: A recent update, J. Drug Deliv. Sci. Technol. (2020). https://doi.org/10.1016/j.jddst.2020.101877.

[17] N. Uchida, M. Yanagi, H. Hamada, Physical enhancement? Nanocarrier? current progress in transdermal drug delivery, Nanomaterials. (2021). https://doi.org/10.3390/nano11020335.

[18] K.B. Vinayakumar, G.M. Hegde, S.G. Ramachandra, M.M. Nayak, N.S. Dinesh, K. Rajanna, Development of cup shaped microneedle array for transdermal drug delivery, Biointerphases. (2015). https://doi.org/10.1116/1.4919779.

[19] K.B. Vinayakumar, G.M. Hegde, M.M. Nayak, N.S. Dinesh, K. Rajanna, Fabrication and characterization of gold coated hollow silicon microneedle array for drug delivery, Microelectron. Eng. (2014). https://doi.org/10.1016/j.mee.2014.05.039.

[20] M. Dehghan, M. Tahmasebipour, S. Ebrahimi, Design, fabrication, and characterization of an SLA 3D printed nanocomposite electromagnetic microactuator, Microelectron. Eng. (2022). https://doi.org/10.1016/j.mee.2021.111695.

[21] R.D. Sochol, E. Sweet, C.C. Glick, S.Y. Wu, C. Yang, M. Restaino, L. Lin, 3D printed microfluidics and microelectronics, Microelectron. Eng. (2018).

https://doi.org/10.1016/j.mee.2017.12.010.

[22] A.I. Bunea, M.H. Jakobsen, E. Engay, A.R. Bañas, J. Glückstad, Optimization of 3D-printed microstructures for investigating the properties of the mucus biobarrier, Micro Nano Eng. (2019). https://doi.org/10.1016/j.mne.2018.12.004.

[23] N. Convery, N. Gadegaard, 30 years of microfluidics, Micro Nano Eng. (2019). https://doi.org/10.1016/j.mne.2019.01.003.

[24] S.R. Dabbagh, M.R. Sarabi, R. Rahbarghazi, E. Sokullu, A.K. Yetisen, S. Tasoglu, 3D-printed microneedles in biomedical applications, IScience. (2021). https://doi.org/10.1016/j.isci.2020.102012.

[25] C. Yeung, S. Chen, B. King, H. Lin, K. King, F. Akhtar, G. Diaz, B. Wang, J. Zhu, W. Sun, A. Khademhosseini, S. Emaminejad, A 3D-printed microfluidic-enabled hollow microneedle architecture for transdermal drug delivery, Biomicrofluidics. (2019). https://doi.org/10.1063/1.5127778.

[26] A.R. Johnson, A.T. Procopio, Low cost additive manufacturing of microneedle masters, 3D Print. Med. (2019). https://doi.org/10.1186/s41205-019-0039-x.

[27] K.J. Krieger, N. Bertollo, M. Dangol, J.T. Sheridan, M.M. Lowery, E.D. O'Cearbhaill, Simple and customizable method for fabrication of high-aspect ratio microneedle molds using low-cost 3D printing, Microsystems Nanoeng. (2019). https://doi.org/10.1038/s41378-019-0088-8.

[28] M. Dalvi, P. Kharat, P. Thakor, V. Bhavana, S.B. Singh, N.K. Mehra, Panorama of dissolving microneedles for transdermal drug delivery, Life Sci. (2021). https://doi.org/10.1016/j.lfs.2021.119877.

[29] S. Sillankorva, L. Pires, L.M. Pastrana, M. Bañobre-López, Antibiofilm Efficacy of the Pseudomonas aeruginosa Pbunavirus vB_PaeM-SMS29 Loaded onto Dissolving Polyvinyl Alcohol Microneedles, Viruses. 14 (2022) 964. https://doi.org/10.3390/v14050964.

[30] Y. Ye, J. Yu, D. Wen, A.R. Kahkoska, Z. Gu, Polymeric microneedles for transdermal protein delivery, Adv. Drug Deliv. Rev. (2018). https://doi.org/10.1016/j.addr.2018.01.015.

[31] J.G. Turner, L.R. White, P. Estrela, H.S. Leese, Hydrogel-Forming Microneedles: Current Advancements and Future Trends, Macromol. Biosci. (2021).

https://doi.org/10.1002/mabi.202000307.

[32] R.F. Donnelly, M.T.C. McCrudden, A.Z. Alkilani, E. Larrañeta, E. McAlister, A.J. Courtenay, M.C. Kearney, T.R. Raj Singh, H.O. McCarthy, V.L. Kett, E. Caffarel-Salvador, S. Al-Zahrani, A.D. Woolfson, Hydrogel-forming microneedles prepared from "super swelling" polymers combined with lyophilised wafers for transdermal drug delivery, PLoS One. (2014). https://doi.org/10.1371/journal.pone.0111547.

[33] K. Ahmed Saeed AL-Japairai, S. Mahmood, S. Hamed Almurisi, J. Reddy Venugopal, A. Rebhi Hilles, M. Azmana, S. Raman, Current trends in polymer microneedle for transdermal drug delivery, Int. J. Pharm. (2020). https://doi.org/10.1016/j.ijpharm.2020.119673.

[34] L.K. Branski, A. Al-Mousawi, H. Rivero, M.G. Jeschke, A.P. Sanford, D.N. Herndon, Emerging infections in burns, Surg. Infect. (Larchmt). (2009). https://doi.org/10.1089/sur.2009.024.

[35] D. Gu, N. Dong, Z. Zheng, D. Lin, M. Huang, L. Wang, E.W.C. Chan, L. Shu, J. Yu, R. Zhang, S. Chen, A fatal outbreak of ST11 carbapenem-resistant hypervirulent Klebsiella pneumoniae in a Chinese hospital: a molecular epidemiological study, Lancet Infect. Dis. (2018). https://doi.org/10.1016/S1473-3099(17)30489-9.

[36] D.M.P. De Oliveira, B.M. Forde, T.J. Kidd, P.N.A. Harris, M.A. Schembri, S.A. Beatson, D.L. Paterson, M.J. Walker, Antimicrobial resistance in ESKAPE pathogens, Clin. Microbiol. Rev. (2020). https://doi.org/10.1128/CMR.00181-19.

[37] H.S. Gill, D.D. Denson, B.A. Burris, M.R. Prausnitz, Effect of microneedle design on pain in human volunteers, Clin. J. Pain. (2008). https://doi.org/10.1097/AJP.0b013e31816778f9.

[38] Y. Bozkurt, E. Karayel, 3D printing technology; methods, biomedical applications, future opportunities and trends, J. Mater. Res. Technol. (2021). https://doi.org/10.1016/j.jmrt.2021.07.050.

[39] A. Sachan, R.J. Sachan, J. Lu, H. Sun, Y.J. Jin, D. Erdmann, J.Y. Zhang, R.J. Narayan, Injection molding for manufacturing of solid poly(l-lactide-co-glycolide) microneedles, MRS Adv. (2021). https://doi.org/10.1557/s43580-021-00030-3.

[40] M. Gülçür, J.M. Romano, P. Penchev, T. Gough, E. Brown, S. Dimov, B. Whiteside, A cost-effective process chain for thermoplastic microneedle manufacture combining laser micro-machining and micro-injection moulding, CIRP J. Manuf. Sci. Technol. (2021).

https://doi.org/10.1016/j.cirpj.2021.01.015.

[41] C.L. Caudill, J.L. Perry, S. Tian, J.C. Luft, J.M. DeSimone, Spatially controlled coating of continuous liquid Interface production microneedles for transdermal protein delivery, J. Control. Release. (2018). https://doi.org/10.1016/j.jconrel.2018.05.042.

[42] S.C. Balmert, C.D. Carey, G.D. Falo, S.K. Sethi, G. Erdos, E. Korkmaz, L.D. Falo, Dissolving undercut microneedle arrays for multicomponent cutaneous vaccination, J. Control. Release. (2020). https://doi.org/10.1016/j.jconrel.2019.11.023.

[43] P. Bhushan, Y. Umasankar, J.D. Hutcheson, S. Bhansali, Toxicity assessment of wearable wound sensor constituents on keratinocytes, Toxicol. Vitr. 58 (2019) 170–177. https://doi.org/10.1016/j.tiv.2019.03.034.

[44] A. de Lacerda Bukzem, D.M. dos Santos, I.S. Leite, N.M. Inada, S.P. Campana-Filho, Tuning the properties of carboxymethylchitosan-based porous membranes for potential application as wound dressing, Int. J. Biol. Macromol. 156 (2021) 459–470. https://doi.org/10.1016/j.ijbiomac.2020.10.204.

[45] E.R. Kenawy, E.A. Kamoun, M.S. Mohy Eldin, M.A. El-Meligy, Physically crosslinked poly(vinyl alcohol)-hydroxyethyl starch blend hydrogel membranes: Synthesis and characterization for biomedical applications, Arab. J. Chem. (2014). https://doi.org/10.1016/j.arabjc.2013.05.026.

[46] Y. Liu, S. Zhou, Y. Gao, Y. Zhai, Electrospun nanofibers as a wound dressing for treating diabetic foot ulcer, Asian J. Pharm. Sci. (2019). https://doi.org/10.1016/j.ajps.2018.04.004.

[47] G. Bonfante, H. Lee, L. Bao, J. Park, N. Takama, B. Kim, Comparison of polymers to enhance mechanical properties of microneedles for bio-medical applications, Micro Nano Syst. Lett. (2020). https://doi.org/10.1186/s40486-020-00113-0.

[48] M.D. Silva, S. Sillankorva, Otitis media pathogens – A life entrapped in biofilm communities, Crit. Rev. Microbiol. (2019) 1–18. https://doi.org/10.1080/1040841X.2019.1660616.

[49] G.J. Noel, A Review of Levofloxacin for the Treatment of Bacterial Infections, Clin. Med. Ther. (2009). https://doi.org/10.4137/cmt.s28.

[50] S.J. Martin, R. Jung, C.G. Garvin, A risk-benefit assessment of levofloxacin in respiratory, skin and skin structure, and urinary tract infections, Drug Saf. (2001).

https://doi.org/10.2165/00002018-200124030-00004.

[51] A.M. Pinto, M.D. Silva, L.M. Pastrana, M. Bañobre-López, S. Sillankorva, The clinical path to deliver encapsulated phages and lysins, FEMS Microbiol. Rev. (2021). https://doi.org/10.1093/femsre/fuab019.

[52] M.S. Arshad, A.T. Zahra, S. Zafar, H. Zaman, A. Akhtar, M.M. Ayaz, I. Kucuk, M. Maniruzzaman, M.W. Chang, Z. Ahmad, Antibiofilm Effects of Macrolide Loaded Microneedle Patches: Prospects in Healing Infected Wounds, Pharm. Res. (2021). https://doi.org/10.1007/s11095-021-02995-0.

[53] X. Yu, J. Zhao, D. Fan, A dissolving microneedle patch for Antibiotic/Enzymolysis/Photothermal triple therapy against bacteria and their biofilms, Chem. Eng. J. 437 (2022) 135475. https://doi.org/10.1016/j.cej.2022.135475.

[54] J.W. Lee, J.H. Park, M.R. Prausnitz, Dissolving microneedles for transdermal drug delivery, Biomaterials. (2008). https://doi.org/10.1016/j.biomaterials.2007.12.048.

[55] B. Xu, G. Jiang, W. Yu, D. Liu, Y. Zhang, J. Zhou, S. Sun, Y. Liu, H2O2-Responsive mesoporous silica nanoparticles integrated with microneedle patches for the glucose-monitored transdermal delivery of insulin, J. Mater. Chem. B. (2017). https://doi.org/10.1039/c7tb02082a.

[56] M.J. Kim, S.C. Park, B. Rizal, G. Guanes, S.K. Baek, J.H. Park, A.R. Betz, S.O. Choi, Fabrication of circular obelisk-type multilayer microneedles using micro-milling and spray deposition, Front. Bioeng. Biotechnol. (2018). https://doi.org/10.3389/fbioe.2018.00054.

[57] T. Waghule, G. Singhvi, S.K. Dubey, M.M. Pandey, G. Gupta, M. Singh, K. Dua, Microneedles: A smart approach and increasing potential for transdermal drug delivery system, Biomed. Pharmacother. (2019). https://doi.org/10.1016/j.biopha.2018.10.078.

[58] J. Sousa, S. Sillankorva, A. Faustino, C. Carvalho, Suggestion for a new bacteriophage genus for the Klebsiella pneumoniae phage vB_KpnS-Carvaje, Curr Genet. 68 (2022) 393–406. https://doi.org/10.1007/s00294-022-01242-2.